

## Learning to See Sharper: A Physics-Informed Artificial Intelligence Framework for Super-Resolving Galaxy Spectra

ARYANA HAGHJOO,<sup>1</sup> SHOUBANEH HEMMATI,<sup>2</sup> BAHRAM MOBASHER,<sup>1</sup> NIMA CHARTAB,<sup>2</sup> ALEXANDER DE LA VEGA,<sup>1</sup>  
TIM EIFLER,<sup>3</sup> EMILY EVERETTS,<sup>4</sup> HOOSHANG NAYYERI,<sup>5</sup> AND ZAHRA SATTARI<sup>2</sup>

<sup>1</sup>*Department of Physics and Astronomy, University of California Riverside, Riverside, CA 92521, USA*

<sup>2</sup>*IPAC, California Institute of Technology, Pasadena, CA 91125, USA*

<sup>3</sup>*The University of Arizona, Tucson, AZ 85721, USA*

<sup>4</sup>*Department of Astronomy, University of California Berkeley, Berkeley, CA 94720, USA*

<sup>5</sup>*Amazon*

### ABSTRACT

The information recoverable from galaxy spectra depends fundamentally on spectral resolution, yet assembling large samples at high resolution remains observationally expensive. We present a deep-learning framework for spectral super-resolution that enhances low-resolution galaxy spectra by a factor of  $\sim 10$  in resolving power ( $R \sim 100$  to  $R \sim 1000$ ). The model is trained on 1,187 paired JWST/NIRSpec observations from the JADES program, where low-resolution prism spectra are matched with medium-resolution grating spectra (G140M, G235M, G395M) combined into a unified reference covering 1–5  $\mu\text{m}$ . Our three-stage architecture performs an initial super-resolution, infers the redshift from the coarse reconstruction, and then applies a physics-informed residual refinement that uses attention across emission-line tokens to learn inter-line relationships and predict parametric line profiles, alongside a convolutional branch for continuum corrections. Evaluated on a 20% held-out sample, the model achieves noise-limited residuals over most of the spectral range and systematically improves the signal-to-noise ratio of key diagnostic lines including [O II], H $\beta$ , [O III], and H $\alpha$ , often by factors of several. The super-resolved spectra successfully deblend features that are entirely unresolved at prism resolution, such as the [O III]  $\lambda\lambda 4959, 5007$  doublet and H $\beta$ . As a proof of concept using JWST data, this approach is readily extensible to the low-resolution grism spectroscopy that will be delivered by *Euclid* and the *Roman Space Telescope*, potentially enabling population-level diagnostics across millions of galaxy spectra that would otherwise be inaccessible at grism resolution.

*Keywords:* galaxies:, methods: data analysis, methods: statistical

### 1. INTRODUCTION

The information content recoverable from galaxy light is fundamentally set by the resolution at which it is observed. From broadband photometry through narrow-band imaging to spectroscopy, progressively finer spectral features become accessible, and with them a more informative set of physical diagnostics. Emission lines detected in galaxy spectra provide a wealth of information: precise redshifts for cosmological analyses such as galaxy clustering and weak lensing (e.g., Hemmati et al. 2019; Wang et al. 2019; Adame et al. 2025), and mea-

surements of physical properties including dust attenuation from the Balmer decrements (e.g., Shivaie et al. 2016), star-formation rate (e.g., Khostovan et al. 2024; Woodrum et al. 2025; Shen et al. 2025), gas-phase metallicity (e.g., Shivaie et al. 2020; Alavi et al. 2026), AGN activity via BPT diagnostics (e.g., Baldwin et al. 1981; Kewley et al. 2006; Agostino et al. 2023), kinematics (e.g., Schreiber et al. 2009; Price et al. 2020), and electron density from [S II] line ratios (e.g., Donald & Osterbrock 2005; Darvish et al. 2015). However, many of these measurements depend on well-resolved lines that are close in wavelength, such as H $\alpha$  and [N II] (e.g., Sobral et al. 2009; Faisst et al. 2018; Martens et al. 2019), or faint features such as the [O I] shock tracer associated with stellar winds and outflows (e.g., Ji et al. 2020;

Hartigan et al. 2004). When the spectral resolution is insufficient, these lines blend together, propagating systematic biases into every derived quantity, from the redshifts that underpin cosmological constraints to the dust corrections and star-formation rates that govern our understanding of galaxy evolution. Achieving the full scientific return of spectroscopic surveys therefore demands high spectral resolution. Equally important are large samples that capture the diversity of galaxy populations and distinguish genuine physical correlations from stochastic variations.

Assembling large spectroscopic samples that simultaneously achieve high spectral resolution, wide area coverage, and sufficient depth remains one of the key observational challenges in extragalactic astronomy. Each current and forthcoming facility navigates a different compromise among these requirements. Ground-based surveys such as SDSS (Kollmeier et al. 2026) and DESI (Martini et al. 2018) cover wide areas at moderate-to-high spectral resolution, but are limited in depth and therefore probe primarily the low-redshift Universe. Space-based survey missions such as *Euclid* (Laureijs et al. 2010) and the forthcoming *Roman Space Telescope* (Spergel et al. 2013; Schlieder et al. 2024) reach fainter galaxies over vast areas, but rely on slitless grism spectroscopy that provides only low spectral resolution, trading resolving power for survey volume. *James Webb Space Telescope* (JWST; Gardner et al. 2006), by contrast, offers high spectral resolution, but its limited field of view restricts it to targeted observations rather than wide-area surveys. As a result, no single facility currently delivers high-resolution spectra for statistically large samples at high redshift, and therefore, cosmological probes such as galaxy clustering and weak lensing must contend with either blended emission lines or limited sample sizes.

One way to circumvent this trade-off is to leverage the small but growing number of galaxies observed at both low and high spectral resolution, and use machine learning to learn the mapping between the two, enabling the resolution enhancement of the much larger low-resolution samples. Machine-learning methods have already demonstrated success across a range of astronomical applications, from imaging super-resolution and source deblending to galaxy classification and the estimation of physical parameters (e.g., Djorgovski et al. 2022; Hemmati et al. 2022; Sanjaripour et al. 2024; Parker et al. 2024; Doorenbos et al. 2024; Parker et al. 2025; Hemmati et al. 2026). However, the application of such techniques to spectral resolution enhancement, that is, learning to recover fine spectral features from low-resolution data, remains largely unexplored. In this

work, we develop a deep-learning-based spectral super-resolution framework that enhances low-resolution near-infrared galaxy spectra to medium spectral resolution, effectively reconstructing important diagnostic features that would otherwise be blended.

The model is trained on paired spectra from the *JWST Advanced Deep Extragalactic Survey* (JADES; Eisenstein et al. 2023), where low-resolution prism observations ( $R \sim 100$ ) are matched with medium-resolution grating spectra (G140M, G235M, G395M;  $R \sim 1000\text{--}2700$ ) of the same galaxies. By learning from these paired samples, augmented with noise and redshift perturbations, the network captures physically meaningful mappings between low- and higher-resolution spectral representations. In this proof of concept study, we use JWST prism and grating data, but the approach is also applicable to the low-resolution grism spectroscopy delivered by wide-area cosmological surveys such as *Euclid* and the *Roman Space Telescope*, potentially enabling population-level diagnostics that would otherwise be inaccessible at grism resolution.

The paper is organized as follows. §2 describes the JADES spectral data used in this study. §3 outlines our methodology, including data preprocessing, augmentation, and the model architecture and training procedure. §4 presents results and evaluation of our super-resolution model. Finally, §5 discusses the implications of this work and avenues for future improvement.

## 2. THE JADES DATASET

For a comprehensive description of the JADES, we refer the reader to Eisenstein et al. 2023; Rieke et al. 2023; Bunker et al. 2024; Eisenstein et al. 2025; D’Eugenio et al. 2025; Curtis-Lake et al. 2025. Briefly, JADES provides deep imaging and spectroscopy in the GOODS-North and GOODS-South fields (Giavalisco et al. 2004), combining Near-InfraRed Camera (NIRCam) and Near-InfraRed Spectrograph (NIRSpec) observations that span from rest-frame ultraviolet to near-infrared. The complete JADES spectroscopic sample (Data Release 4; Curtis-Lake et al. 2025) consists of 5,190 targets, of which 3,297 have robust spectroscopic redshifts extending to  $z \sim 14$ .

What makes the JADES particularly suited to this work is the tiered survey design that pairs low-resolution prism observations ( $R \sim 30\text{--}300$ ) with medium-resolution grating modes ( $R \sim 1000$ ; G140M, G235M, and G395M) for the same targets. The survey architecture balances depth and area: Deep and Ultra-Deep tiers comprise  $\sim 700$  galaxies with 20–50 hour integrations in the prism mode, while Medium tiers include over 4,400 galaxies with shallower 1–3 hour exposures. This di-

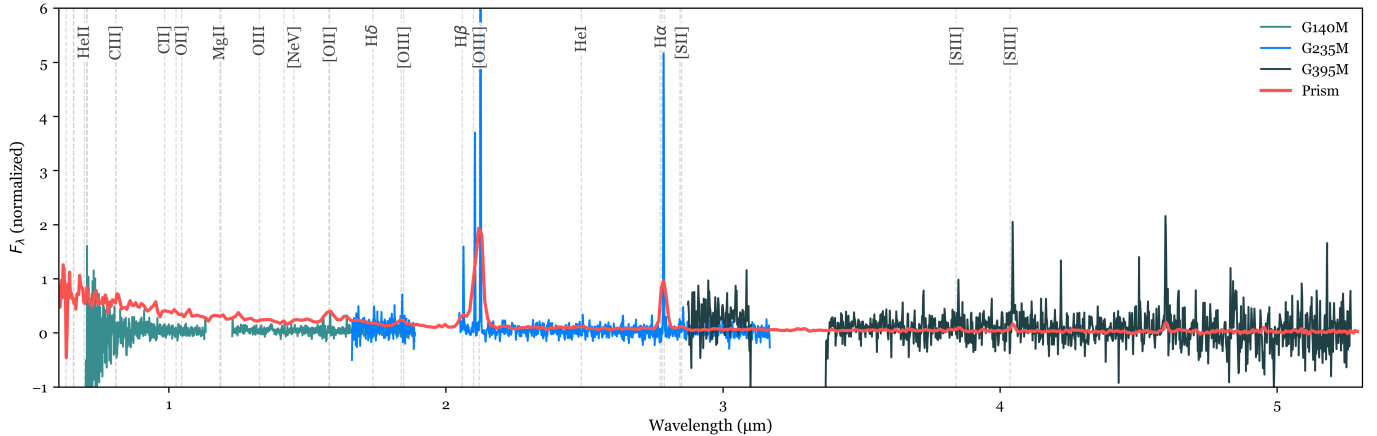


**Figure 1.** Example low- and medium-resolution JWST NIRSpec spectra for a representative JADES galaxy. The prism spectrum is shown in red, and the medium-resolution G140M, G235M, and G395M segments are overplotted in green, blue, and black, respectively. The natural gaps and overlaps between the three medium-resolution gratings are evident across the wavelength range. Vertical dashed lines mark key emission lines commonly utilized in nebular and galaxy evolution studies, shifted to the observed frame at the galaxy’s redshift ( $z = 3.235$ ). All spectra are normalized to allow visual comparison.

versity ensures the training set covers a wide dynamic range in signal-to-noise. An example of the prism and medium-resolution spectra for a representative JADES galaxy is shown in Figure 1.

The prism observations capture the full  $0.6\text{--}5.3\ \mu\text{m}$  wavelength range, while the medium-resolution gratings extend coverage to  $5.5\ \mu\text{m}$ , together providing access to key diagnostic lines such as  $\text{H}\alpha$ ,  $\text{H}\beta$ ,  $[\text{O III}]$ ,  $[\text{N II}]$ , and  $[\text{S II}]$ . The low resolving power of the prism results in the blending of critical features, including  $\text{H}\alpha\text{--}[\text{N II}]$ ,  $[\text{O III}]$ , and the  $[\text{O II}]$  and  $[\text{S II}]$  doublets. In contrast, the medium-resolution gratings resolve these lines individually. By combining the three grating modes, we construct a single medium-resolution reference spectrum covering  $1\text{--}5\ \mu\text{m}$ , which serves as the high-resolution target for model training. As noted in §1, the broad wavelength coverage of the JADES training data makes this framework readily extendable to low-resolution grism spectroscopy from missions such as the *Euclid* and *Roman Space Telescope*.

### 3. METHODOLOGY

Our spectral super-resolution framework is described in four parts: *preprocessing* (§3.1), *augmentation* (§3.2), *model architecture and training* (§3.3), and *hyperparameter optimization* (§3.4).

#### 3.1. Pre-processing

The JADES dataset provides low-resolution *prism* spectra and three medium-resolution grating spectra for an overlapping subset of galaxies. To construct training pairs suitable for spectral super-resolution, we preprocess the data through source matching, medium-resolution spectrum construction, wavelength align-

ment, and quality filtering. The goal of this pipeline is to produce wavelength-aligned low- and medium-resolution spectra that are directly comparable.

We first cross-identify galaxies observed in both *prism* mode and the medium-resolution gratings. Sources are matched using right ascension, declination, and field identifiers, and a match is accepted only if the angular separation is below 0.2 arcsec, conservatively larger than JWST’s absolute astrometric accuracy of  $\sim (0.02\text{--}0.03)$  arcsec (Lallo & Hartig 2022). For each matched galaxy, we adopt the spectroscopic redshift measured from the medium-resolution data in the JADES catalogs.

For every matched object, the three medium-resolution grating spectra (G140M, G235M, G395M) are then merged into a single continuous spectrum. In wavelength regions where adjacent gratings overlap, relative flux scale factors are computed by minimizing the RMS flux difference within the overlap. These scale factors are applied to place all gratings on a consistent flux scale, after which small residual discontinuities at grating boundaries are corrected and the spectra are concatenated. This procedure yields a stitched medium-resolution spectrum with a corresponding uncertainty array.

We next align the prism and medium-resolution spectra onto a common wavelength grid. The unified grid is defined by the native sampling of the medium-resolution data, ensuring that the intrinsic spectral resolution of the grating spectra is preserved. The stitched medium-resolution spectrum already lies on this grid, while the prism spectrum is *up-sampled* to the same wavelength points using cubic interpolation. We choose cubic over

linear interpolation because it produces smoother flux profiles that better preserve the shape of broad spectral features, while still not introducing artificial high-frequency structure into the low-resolution data. Both prism fluxes and flux uncertainties are interpolated to the unified grid. This step does not introduce additional spectral information into the prism data; it merely evaluates the observed low-resolution spectrum on the high-resolution wavelength grid.

Finally, we apply a quality cut based on the signal-to-noise ratio (S/N) of certain spectral features to define the training sample. Galaxies are retained only if their medium-resolution spectrum shows at least one significant detection of H $\alpha$ , [O II], or [O III] with S/N > 5. We adopt a deliberately low threshold to maximize the training sample size while still ensuring that each spectral pair contains at least one real emission feature, preventing the model from learning spurious emission features in noise-dominated spectra.

For each galaxy that passes all selection criteria, the pipeline outputs a standardized data product consisting of the up-sampled prism flux and uncertainty on the unified wavelength grid, the stitched medium-resolution flux and uncertainty on the same grid, and associated metadata including sky coordinates, redshift, and unique identifiers. These wavelength-aligned, quality-filtered spectral pairs form the final dataset used for augmentation and model training in the following sections.

### 3.2. Augmentation

Following pre-processing, a data augmentation procedure is applied to increase the size and diversity of the training set. The initial dataset consists of 1,187 matched pairs of low-resolution prism spectra and corresponding medium-resolution spectra. For each original pair, we generate 20 stochastic realizations, which together with the original spectra result in a final augmented dataset of 24,927 paired spectra.

As illustrated in Figure 2, each augmented realization is produced by applying small random redshift and flux perturbations to both the low- and high-resolution spectra. Redshift offsets are drawn from a Gaussian distribution in redshift space,  $z_{\text{shift}} \sim \mathcal{N}(0, \sigma_z)$  with  $\sigma_z = 0.3$ , and are applied by remapping wavelengths from the original to the perturbed redshift. This introduces small continuous shifts in the apparent positions of emission features, encouraging the network to learn representations that are robust to line-position variability rather than relying on fixed grid locations.

To further emulate observational variability, Gaussian noise is added independently to the low- and high-

resolution spectra. The noise amplitude is scaled to 10% of the flux value at each wavelength. Applying independent noise realizations to the input and target spectra prevents the network from simply learning to copy the input to the output, and instead forces it to recover stable high-resolution features in the presence of flux uncertainties.

After redshift and noise perturbations, all spectra are trimmed to a common wavelength range of 1–5  $\mu\text{m}$  to ensure uniform coverage across the dataset and to exclude low-sensitivity detector edges.

The choice of 20 augmented realizations per spectrum reflects a practical balance between dataset expansion and information content. Empirically, increasing the number of augmentations beyond this point does not lead to measurable improvements in training stability or validation performance, indicating saturation in the effectiveness of additional stochastic variants. This strategy expands the training set by more than an order of magnitude while ensuring that the model continues to learn physically meaningful mappings between low- and high-resolution spectra.

### 3.3. Model Architecture and Training

Recovering high-resolution spectral structure from low-resolution observations is an intrinsically ill-posed problem. Narrow emission and absorption features are sparse, redshift-dependent, and often comparable in amplitude to instrumental noise, making them difficult to distinguish from statistical fluctuations. End-to-end super-resolution models trained directly from low- to high-resolution spectra tend to either oversmooth physically real features or hallucinate sharp lines that are inconsistent with any plausible spectroscopic interpretation. To address these challenges, we adopt a staged architecture that explicitly separates coarse reconstruction, physical interpretation, and fine-scale refinement. An overview of the full three-stage pipeline is shown in Figure 3.

The first stage (hereafter SR1) performs a conservative super-resolution of the low-resolution spectrum onto a fixed, high-resolution wavelength grid. The goal of SR1 is not to recover the sharpest possible spectral features, but rather to reconstruct the global continuum shape and broad spectral structure in a stable and noise-robust manner. This stage provides a physically reasonable baseline spectrum that preserves large-scale flux relationships while avoiding the introduction of spurious fine-scale structure. In this sense, SR1 serves as a learned interpolation that respects the statistical properties of the input data.

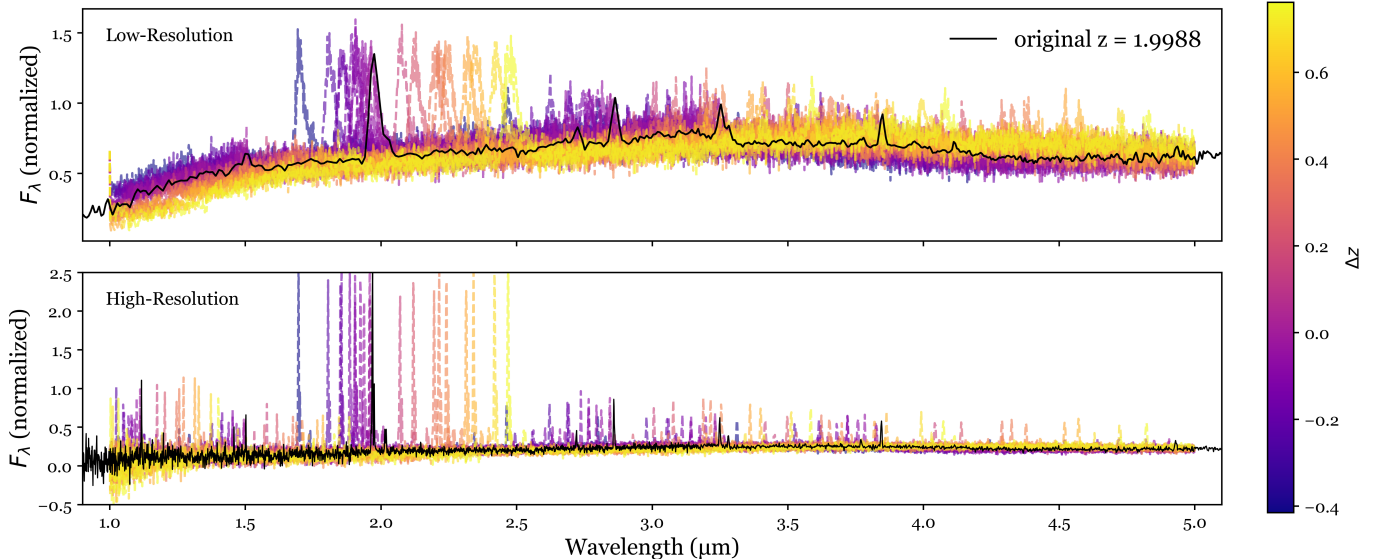


**Figure 2.** Example of the data augmentation procedure applied to a matched pair of low- and high-resolution JADES spectra. *Top:* the original low-resolution prism spectrum (solid black) and twenty augmented realizations (colored dashed curves) generated by applying Gaussian-distributed redshift offsets ( $z_{\text{shift}} \sim \mathcal{N}(0, \sigma_z)$  with  $\sigma_z = 0.3$ ) and flux perturbations scaled to 10% of the local flux. *Bottom:* the corresponding high-resolution spectrum with independent realizations of the same stochastic perturbations. These augmentations introduce realistic variations in line positions and amplitudes while preserving the underlying astrophysical structure, thereby expanding the training set and promoting shift-robust, noise-tolerant learning.

Both SR1 and subsequent stages predict wavelength-dependent uncertainties in addition to the reconstructed flux. This heteroscedastic formulation reflects the fact that spectroscopic noise varies across the detector bandpass and that the high-resolution training targets may themselves contain residual calibration artifacts or measurement uncertainties. Explicit uncertainty modeling prevents the network from being overly penalized for failing to reproduce features that are not statistically supported by the data and enables downstream components to reason about which deviations are physically meaningful.

In the second stage, a dedicated redshift inference network is applied to the output of SR1. This network is trained in a supervised manner using labeled redshift values. Redshift is treated as a global latent parameter that constrains the relative spacing and identity of spectral features across the full wavelength range. Inferring redshift explicitly allows the model to capture long-range spectral coherence that is difficult to enforce using purely local convolutional operations. During training, the predicted redshifts exhibit substantial scatter and systematic bias in early epochs, when the SR1 reconstruction is still coarse; as the super-resolution backbone converges, the redshift predictions tighten markedly around the one-to-one relation, with reduced normalized error  $|\Delta z|/(1+z)$ . This progression demonstrates that reliable redshift estimates can be obtained directly from the coarse super-resolved spectra

and that improvements in spectral reconstruction translate into improved global parameter inference.

Crucially, redshift inference is performed prior to fine-scale spectral refinement. This ordering mirrors standard spectroscopic analysis, in which an approximate redshift hypothesis is formed before individual features are interpreted. By conditioning later refinement on an explicit redshift estimate, the model is encouraged to distinguish between features that form a coherent line system and those that are more consistent with noise.

Using the inferred redshift, a soft, wavelength-dependent line mask is constructed by shifting a rest-frame emission-line list into the observed frame. The resulting mask highlights regions of the spectrum where spectral lines are physically plausible, with a finite width that reflects instrumental resolution and redshift uncertainty. This mask does not enforce the presence of specific lines; rather, it encodes physical plausibility in a probabilistic manner that can be incorporated into the refinement process.

The third stage (SR2) refines the SR1 output by predicting a residual correction rather than a full reconstruction. SR2 is conditioned on the coarse spectrum, its associated uncertainty, the redshift-informed line mask, and the inferred redshift itself. Unlike the purely convolutional SR2 described in earlier iterations of this work, the refinement network adopts a two-branch architecture that separates emission-line modeling from smooth continuum correction, reflecting the physical decompo-

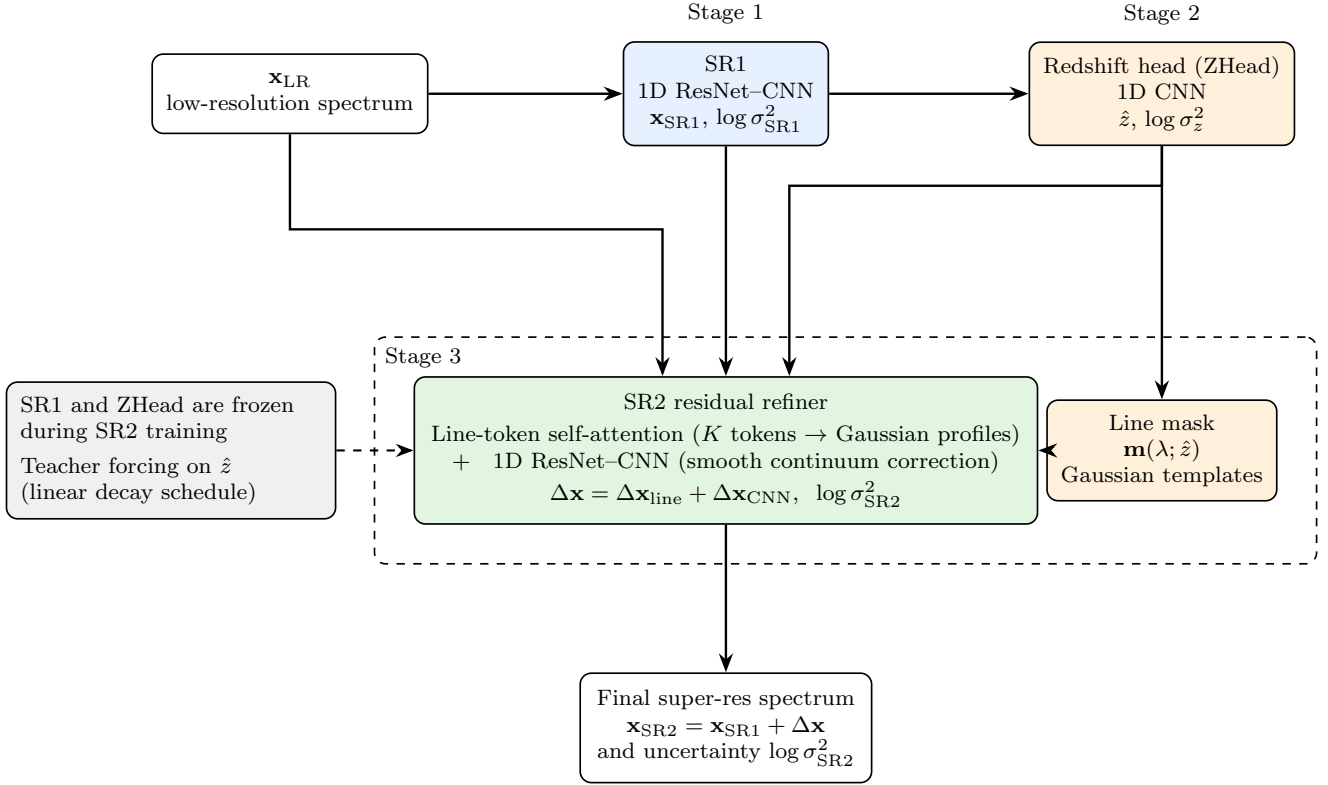


**Figure 3.** Schematic of the three-stage physics-informed spectral super-resolution framework. Stage 1 (SR1) maps the low-resolution input spectrum to an initial super-resolved estimate and predictive uncertainty. Stage 2 (ZHead) infers redshift from the SR1 representation. Stage 3 (SR2) refines SR1 via two parallel internal branches: a *line-token self-attention* branch that extracts local spectral windows at the  $\hat{z}$ -predicted positions of  $K$  known rest-frame emission lines, applies multi-head self-attention across all line tokens, and predicts parametric Gaussian profiles gated by a learned presence probability; and a *residual CNN* branch for smooth continuum corrections. The two residuals are summed to produce  $\Delta \mathbf{x} = \Delta \mathbf{x}_{\text{line}} + \Delta \mathbf{x}_{\text{CNN}}$ . The inferred redshift  $\hat{z}$  enters Stage 3 through two paths: it determines the pixel positions at which local spectral windows are extracted for the line tokens, and it defines the redshift-conditioned emission-line mask. During training, teacher forcing linearly decays the probability of substituting the catalog redshift for  $\hat{z}$ . Dashed arrows denote training-objective connections rather than forward inference.

sition of galaxy spectra into a slowly varying continuum plus discrete spectral features.

The first branch is a physics-informed line modeler built around multi-head self-attention. For each of  $K$  known rest-frame emission lines, the inferred redshift  $\hat{z}$  is used to compute the expected observed-frame wavelength, and a local spectral window of  $2W + 1$  pixels is extracted from the input channels centered on that position. Each window is encoded by a small convolutional network with multi-scale adaptive pooling, producing a compact feature vector per line. A learnable identity embedding, unique to each rest-frame line species, is added to the encoded representation, allowing the network to distinguish lines with similar local spectral morphology (e.g., the two components of a doublet) on the basis of their physical identity.

The resulting set of  $K$  line tokens is then processed by a Transformer encoder consisting of multiple multi-head self-attention layers. This cross-attention mech-

anism allows every line token to exchange information with every other, enabling the network to learn inter-line relationships such as the fixed  $\sim 1:3$  flux ratio of the [O III]  $\lambda\lambda 4959, 5007$  doublet, the Balmer decrement linking  $\text{H}\alpha$  and  $\text{H}\beta$ , and correlations between ionization-sensitive line groups. These relationships provide powerful physical constraints that a purely local convolutional architecture cannot capture, because the relevant lines may be separated by hundreds of pixels in the observed frame.

Each line token is then decoded into a parametric Gaussian profile. Separate linear heads predict the amplitude, log-width, and sub-pixel wavelength offset of each line, as well as a presence probability obtained via a sigmoid gate. The presence gate allows the network to suppress lines that are not supported by the data rather than forcing every known line to appear, preventing hallucination. Lines whose predicted observed wavelength falls outside the spectral range are additionally

masked. The full line-branch residual is reconstructed as a sparse sum of Gaussians, each deposited at the predicted position with the predicted width and gated amplitude. This parametric formulation ensures that the line corrections are physically interpretable—each predicted line has a well-defined identity, position, width, and strength—and produces sparse, localized modifications to the spectrum rather than diffuse adjustments.

The second branch is a shallow residual convolutional network that predicts a smooth continuum correction. This branch operates on the same concatenated input channels as the line branch but uses a small number of residual blocks with moderate channel width, biasing it toward low-frequency adjustments. The residual blocks employ scaled skip connections (with a factor of 0.5) to further constrain the magnitude of continuum corrections. The two branches are summed to produce the total residual prediction:  $\Delta x = \Delta x_{\text{line}} + \Delta x_{\text{CNN}}$ , and the final super-resolved spectrum is  $x_{\text{SR2}} = x_{\text{SR1}} + \Delta x$ . A separate convolutional head predicts wavelength-dependent log-variance from the input channels.

Refinement is guided by loss terms that emphasize high-frequency spectral components corresponding to narrow lines and sharp features. High-pass filtered components of the refined spectrum are encouraged to match those of the high-resolution target preferentially within the line mask, while regions outside the mask are biased toward smoothness and minimal deviation from the coarse reconstruction. This asymmetric treatment reflects the physical expectation that genuine high-frequency structure should be concentrated near spectral lines, whereas the continuum should remain smooth. Additional regularization terms discourage the amplification of noise-like residuals in regions without physical justification.

All three components of the pipeline are implemented as one-dimensional neural networks operating along the wavelength axis. SR1 and the CNN branch of SR2 use convolutional architectures that reflect the inherently ordered and local nature of spectroscopic data, while the line-attention branch of SR2 uses a Transformer encoder that captures long-range inter-line correlations. One-dimensional convolutions provide translational equivariance along the spectral axis while avoiding the unnecessary complexity of two-dimensional architectures designed for imaging applications. The full three-stage pipeline totals approximately 2.5 million trainable parameters, comparable in scale to lightweight mobile vision architectures such as MobileNet (Howard et al. 2017), and well-matched to the dataset size of a few thousand spectra without requiring aggressive regularization to prevent overfitting.

The initial super-resolution network (SR1) adopts a residual convolutional architecture composed of a shallow input projection followed by a stack of residual blocks with small convolutional kernels. Each block consists of normalized convolutional layers with nonlinear activations and skip connections, allowing the network to increase effective depth while maintaining stable gradient flow. This design enables SR1 to model broad continuum structure and blended features without aggressively amplifying noise. The final layers predict both the reconstructed flux and a wavelength-dependent log-variance, enabling uncertainty estimation.

Across all stages, residual connections are used both within individual networks and between stages of the pipeline. This hierarchical residual structure reflects the physical intuition that high-resolution spectra can be decomposed into a smooth continuum plus localized deviations associated with spectral features. By enforcing this decomposition architecturally, the model is biased toward physically interpretable solutions and away from unconstrained hallucination.

Training proceeds sequentially: SR1 is trained first and frozen, followed by the redshift inference network, and finally the SR2 refinement stage. Freezing earlier components ensures that later optimization does not distort physically interpretable quantities, such as redshift, in order to minimize pixel-level reconstruction losses. During SR2 training, a teacher-forcing schedule is employed in which the true catalog redshift is substituted for the inferred  $\hat{z}$  with a probability that decays linearly from 0.8 to 0.2 over the course of training. In early epochs, this provides the line-attention branch with accurate line positions, allowing it to learn profile shapes and inter-line relationships before being exposed to the full noise of the redshift inference; as training progresses, the model is increasingly required to operate on its own redshift estimates, ensuring robustness at inference time. This staged training strategy stabilizes convergence and preserves the interpretability of intermediate representations.

The effectiveness of the full pipeline is illustrated in Figure 4, which compares low-resolution input spectra to the refined super-resolution spectra and against high-resolution targets. The examples demonstrate that the three-stage architecture sharpens physically meaningful spectral features while maintaining conservative behavior in regions lacking strong physical support for fine-scale structure.

### 3.4. Hyperparameter Optimization

To identify optimal configurations for each stage of the super-resolution pipeline, we performed three sequential

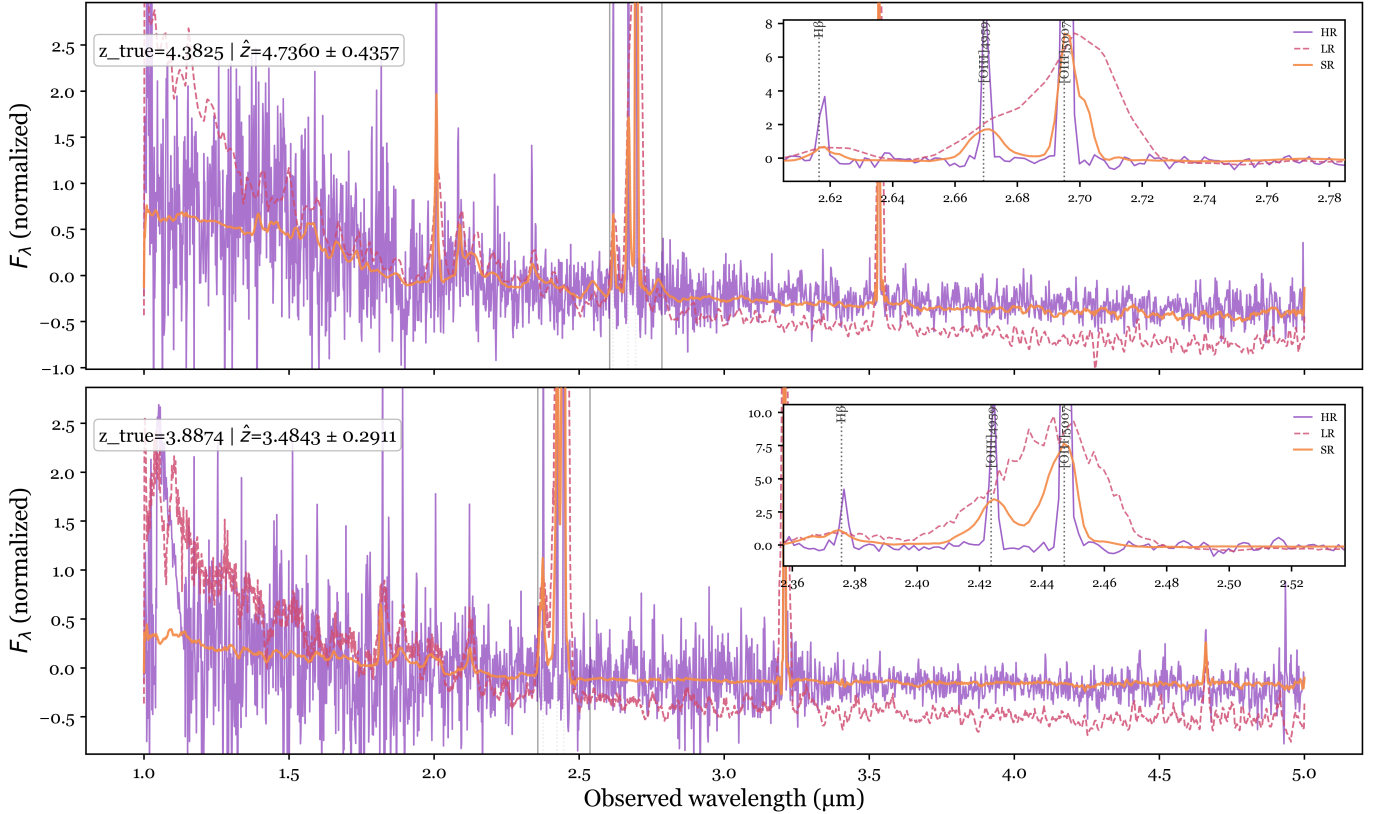


**Figure 4.** Example galaxy spectra illustrating the performance of our super-resolution model. For each system, the low-resolution *prism* input (purple) and the corresponding super-resolved output (orange) are shown across the full 1–5  $\mu\text{m}$  wavelength range. Both examples are taken from the 20% evaluation split and were never used during training. Vertical dashed lines mark the expected observed-frame positions of prominent emission features (e.g. [O II], H $\beta$ , [O III], H $\alpha$ ), with labels shown above each line. In both galaxies, the model successfully reconstructs narrow emission-line peaks at the correct wavelengths even when the low-resolution spectra exhibit only blended or low-S/N structure. These examples demonstrate the model’s ability to recover physically meaningful, high-resolution spectral features directly from *prism*-resolution data.

Bayesian hyperparameter sweeps using the Weights & Biases (W&B) framework (Biewald 2020). Each sweep explored a multi-dimensional space including the learning rate, weight decay, dropout probability, hidden-layer dimensionality, number of residual blocks, activation function, gradient clipping, and batch size. For the SR2 refinement stage, the search space additionally included the line-token embedding dimension, number of attention heads and layers, spectral window half-width, CNN branch depth and channel width, the residual magnitude cap, and the L1 penalty on residual amplitude. All trials within each sweep were trained using identical data splits and preprocessing to ensure controlled comparison.

The first sweep optimized SR1, the coarse super-resolution network. Once the best SR1 configuration was identified, that model was frozen and used as input to the second sweep, which optimized the redshift inference network. Finally, with both SR1 and the redshift network frozen at their optimal configurations, a

third sweep was performed to optimize the SR2 refinement stage. This sequential approach mirrors the staged training procedure and ensures that each component is tuned in the context in which it will be deployed.

Figure 5 summarizes the results from the SR1 sweep in a parallel-coordinates representation, where each line corresponds to a single trained model and the color encodes the average validation loss. The lowest-loss configurations cluster around *ELU* activations, moderate learning rates of a few  $\times 10^{-4}$ , non-zero dropout, and deeper architectures with  $\sim 8$  residual blocks. Shallower networks consistently underperformed, while excessively large hidden dimensions did not yield additional gains and occasionally introduced training instability. Sweep results for the redshift inference and SR2 refinement networks exhibit similar trends and are not shown separately.

Parameter importance analysis reveals distinct sensitivities across the three stages. For SR1, the most influential hyperparameters are the loss weighting terms

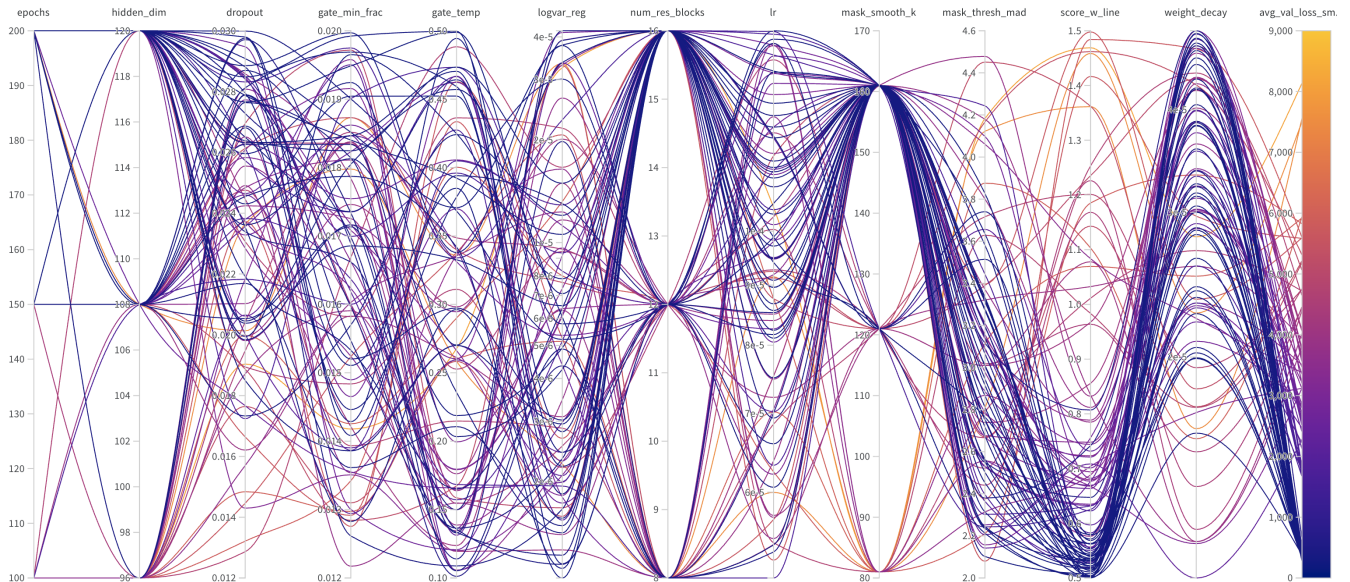


**Figure 5.** Parallel-coordinates visualization of the W&B Bayesian hyperparameter sweep. Each polyline corresponds to a single trained model, with color indicating the average validation loss. The lowest-loss configurations cluster toward *ELU* activations, a hidden dimension of  $\sim 128$ , batch size 16, learning rates of a few  $\times 10^{-4}$ , non-zero dropout, and deeper architectures with  $\sim 8$  residual blocks. These trends motivated the final network design and training configuration adopted in this work.

that balance reconstruction fidelity near spectral lines against continuum smoothness. This reflects the fundamental challenge of super-resolution: the network must learn where to sharpen features versus where to remain conservative, and this trade-off is encoded directly in the loss function rather than emerging automatically from architectural choices.

In contrast, the redshift inference network shows greatest sensitivity to learning rate and dropout. This likely reflects the inherently global nature of redshift estimation, which requires integrating information across many spectral features simultaneously. The network must learn subtle correlations between distant wavelength regions while avoiding overfitting to individual noisy features, a task that is highly sensitive to regularization strength and optimization dynamics. Learning rate becomes critical because redshift inference involves compressing high-dimensional spectral information into a single scalar value, requiring careful balancing of gradient magnitudes across the network depth.

For the SR2 refinement stage, parameter importance is dominated by the residual constraint hyperparameters: the magnitude cap applied to the predicted residual and the L1 penalty on its amplitude. Both act to limit how far the refined spectrum may deviate from the SR1 baseline, and their strong influence reflects the central design tension of the refinement stage, allowing sufficient flexibility to recover genuine spectral features while preventing unconstrained modification of the coarse reconstruction. As with the earlier stages, architectural

parameters such as the attention embedding dimension, number of heads, and CNN depth show comparatively minor influence.

Notably, across all three stages, architectural parameters such as network depth and hidden dimension show relatively minor impact, suggesting that the model capacity required for these tasks is easily satisfied by most reasonable architectures. This finding underscores that careful tuning of the training procedure and physically motivated loss function design are more critical to performance than simply scaling model capacity.

All models were implemented in PyTorch and trained on an NVIDIA GeForce RTX 5090 GPU. Each hyperparameter sweep consisted of approximately 100–150 trials, with individual runs typically completing within 1–2 hours. The complete hyperparameter optimization across all three stages required approximately 400 GPU-hours. Final models trained with optimal configurations converged within 50–100 epochs, requiring 2–4 hours per stage.

#### 4. RESULTS

We evaluate the performance of our super-resolution model on a 20% held-out subset of the JADES sample that was never seen during training. The model successfully recovers narrow emission-line features from low-resolution prism inputs, with residuals consistent with the noise properties of the reference spectra and systematic S/N improvements across all diagnostic lines tested. Below, we present representative reconstructions (§4.1),

assess the wavelength-dependent fidelity of the model through residual analysis (§4.2), quantify the improvement in emission-line recoverability (§4.3), and evaluate redshift consistency as a downstream diagnostic of recovered information content (§4.4).

#### 4.1. Generated high-resolution spectra

Figure 4 presents two examples from the 20% held-out evaluation set, selected to illustrate the model’s ability to deblend emission lines that are unresolved at prism resolution. In both cases, the low-resolution prism spectrum (orange) shows a single broad feature in the [O III] region, with a very low S/N  $H\beta$ , and the [O III]  $\lambda 4959$ , and [O III]  $\lambda 5007$  are fully blended. The super-resolved output (green) successfully separates these lines into distinct peaks at the correct observed-frame wavelengths, closely matching the medium-resolution reference spectrum (blue), as shown in the inset panels. The model also recovers the expected  $\sim 1:3$  flux ratio between the [O III] doublet components, indicating that the reconstruction is not only positionally accurate but also physically consistent. These examples demonstrate that the network learns to recover diagnostic structure that is inaccessible at prism resolution.

#### 4.2. Residual Maps

To assess the fidelity of the reconstructed spectra, we examine the residuals between different spectral products and the high-resolution reference spectra. Because galaxies span orders of magnitude in continuum level and emission-line strength, all residual statistics are computed in normalized flux units, using the same per-object normalization applied during training. This removes astrophysical dynamic range from the analysis and places all spectra on a common scale, ensuring that the residuals reflect model performance rather than intrinsic flux diversity.

Figure 6 presents this analysis across the full 20% held-out evaluation set, with galaxies sorted by true redshift along the vertical axis. The top row shows two-dimensional residual maps for three comparisons: the low-resolution input minus the high-resolution reference (LR–HR), the low-resolution input minus the super-resolved output (LR–SR2), and the super-resolved output minus the high-resolution reference (SR2–HR). The LR–HR map reveals strong, coherent residual structure tracing the redshift-dependent positions of emission lines, confirming that these features are present in the HR data but absent or blended in the LR spectra. The LR–SR2 map shows similar structure, indicating that the model successfully introduces emission-line features that were missing in the LR input. In contrast, the

SR2–HR residuals are largely structureless and noise-like, demonstrating that the SR spectra closely match the HR reference across both continuum and line regions.

The bottom row compares the wavelength-dependent reconstruction error, quantified as the robust scatter of the residuals across galaxies ( $\sigma_{\text{resid}}(\lambda)$ ), with the median noise amplitude of the HR data ( $\tilde{\sigma}_{\text{HR,data}}(\lambda)$ ). For the SR2–HR comparison, the two curves converge at wavelengths above  $\sim 2\mu\text{m}$ , indicating that the model achieves noise-limited performance over most of the spectral range. At the bluest wavelengths ( $\lesssim 1.5\mu\text{m}$ ), the reconstruction error exceeds the HR noise floor, consistent with the substantially lower S/N of both the prism input and the HR reference in this regime.

We complement the spatial-domain residual analysis with a frequency-domain diagnostic. Figure 7 shows the power spectral density (PSD) of the high-pass component of the spectra, obtained by subtracting a smoothed continuum, for the LR, SR, and HR products. The left panel reveals that the LR spectra carry excess high-frequency power, dominated by noise and undersampling artifacts, while the HR spectra contain the richest genuine small-scale structure. The SR spectra lie systematically below both, indicating that the model effectively suppresses noise-dominated fluctuations while adopting a conservative reconstruction that avoids injecting spurious fine-scale features. The right panel shows the PSD of the residuals between spectral products. The LR–HR residuals exhibit strong power at all frequencies, reflecting the large difference between prism and grating data. The LR–SR residuals are substantially reduced, confirming that the model removes much of the noise present in the LR input. The remaining SR–HR residual power is smooth and converges toward the noise floor of the HR data at intermediate frequencies, suggesting that further improvement is limited by the quality of the reference spectra rather than by the model itself. Power at the highest frequencies is sensitive to interpolation onto the common wavelength grid and should be interpreted only in a relative sense.

#### 4.3. Emission-Line Recovery

To quantify the recoverability of individual emission features, we fit a Gaussian line model to both the low-resolution *prism* spectra and the super-resolved outputs. For each emission line in a galaxy, we compute the expected observed wavelength from the catalog redshift and extract a narrow window (typically  $\pm 15$ – $20$  pixels) around that position. Within this window, we model

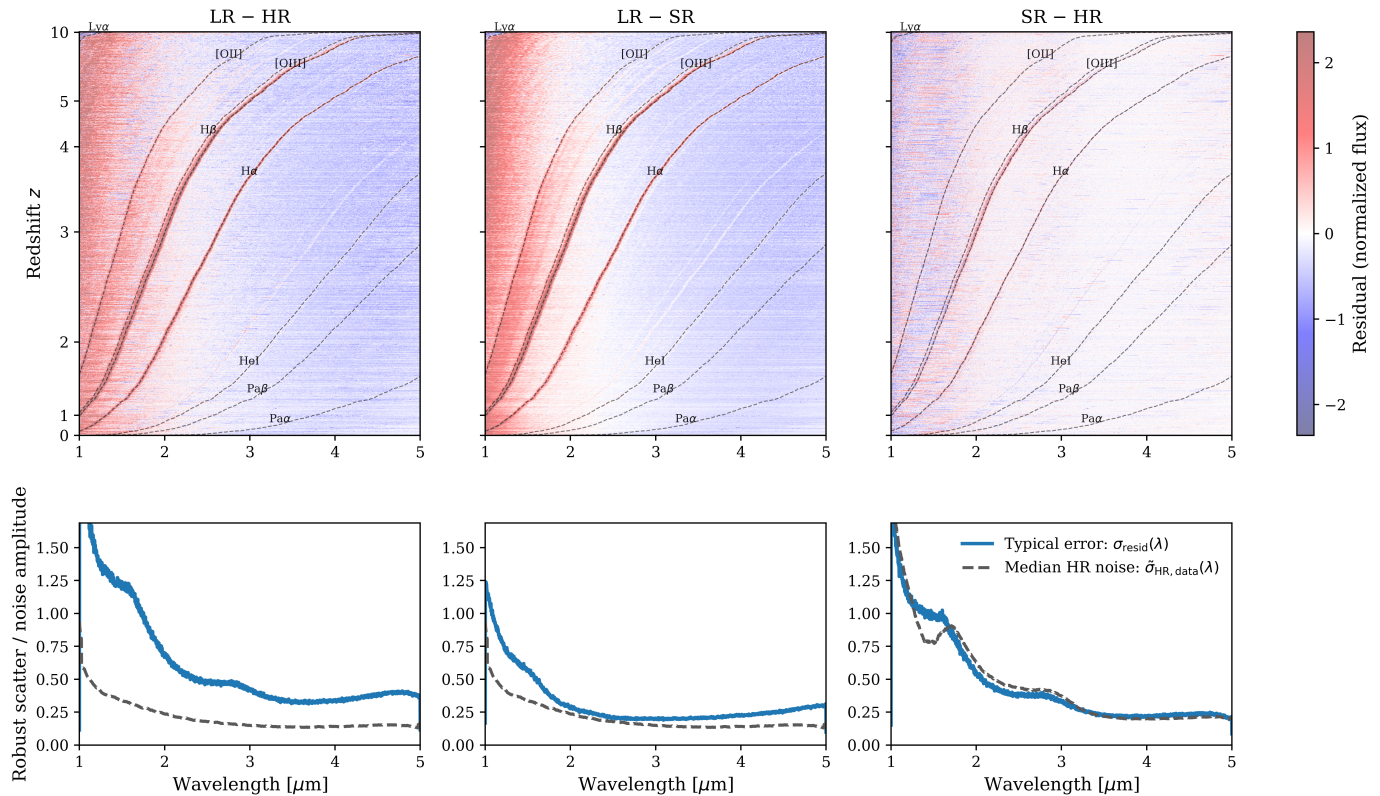


**Figure 6. Residual structure and comparison to data noise.** *Top row:* Residual maps for the same set of galaxies, sorted by true redshift, showing (from left to right) the difference between linearly interpolated low-resolution spectra and high-resolution spectra (LR–HR), low-resolution spectra and the SR2 reconstruction (LR–SR2), and the SR2 reconstruction and high-resolution spectra (SR2–HR). Residuals are shown in normalized flux units and share a common color scale. Coherent wavelength-dependent structure in the LR–HR residuals indicates that low-resolution spectra retain correlated information about high-resolution features, while the SR2–HR residuals are largely structureless and noise-like. *Bottom row:* For each residual map, the solid blue curve shows the typical reconstruction error as a function of wavelength, quantified as the robust scatter (MAD-based standard deviation) of the residuals across galaxies,  $\sigma_{\text{resid}}(\lambda)$ . The dashed gray curve shows the median wavelength-dependent noise amplitude of the input data,  $\tilde{\sigma}_{\text{data}}(\lambda)$ , estimated independently from the spectra via high-frequency residuals after continuum smoothing. For the LR–HR and LR–SR2 panels, the noise estimate is derived from the low-resolution data, while for the SR2–HR panel it is derived from the high-resolution data. Agreement between  $\sigma_{\text{resid}}(\lambda)$  and  $\tilde{\sigma}_{\text{data}}(\lambda)$  indicates noise-limited performance, whereas smaller residual scatter implies implicit denoising by the model.

the observed flux as

$$f(\lambda) = C_0 + C_1\lambda + A \exp\left[-\frac{(\lambda - \mu)^2}{2\sigma^2}\right], \quad (1)$$

where  $A$  is the line amplitude,  $\mu$  the centroid,  $\sigma$  the width, and  $(C_0, C_1)$  describe the local continuum level and slope. The emission-line S/N is defined as  $A/\delta A$ , where  $\delta A$  is the formal uncertainty on the amplitude returned by the covariance matrix of the fit (Haghjoo 2023).

Using this procedure, we compare the S/N measured from the low-resolution *prism* spectra with that measured from the super-resolved outputs across the full evaluation set. Figure 8 summarizes this comparison for four key diagnostic lines: [O II]  $\lambda 3727$ , H $\beta$ , [O III]  $\lambda 5007$ , and H $\alpha$ . For all four lines, the majority of galaxies lie above the one-to-one relation, demonstrating a system-

atic improvement in recovered S/N, often by factors of several. The gains are most pronounced for lines that are heavily blended at prism resolution, such as [O II] and H $\beta$ , where the LR S/N is typically low and the model’s ability to separate features from the continuum yields the largest improvement. A small fraction of galaxies fall near or below the one-to-one line, typically corresponding to cases where the line is intrinsically faint or falls in a low-sensitivity region of the detector.

The physical origin of the S/N improvement is straightforward: by concentrating flux into a narrower line profile and reducing effective continuum noise within the fitting window, the SR outputs yield higher-amplitude, better-constrained Gaussian fits. These gains are especially important for faint or high-redshift galaxies, where crucial diagnostic features are intrinsically weak or unresolved in the native prism data.

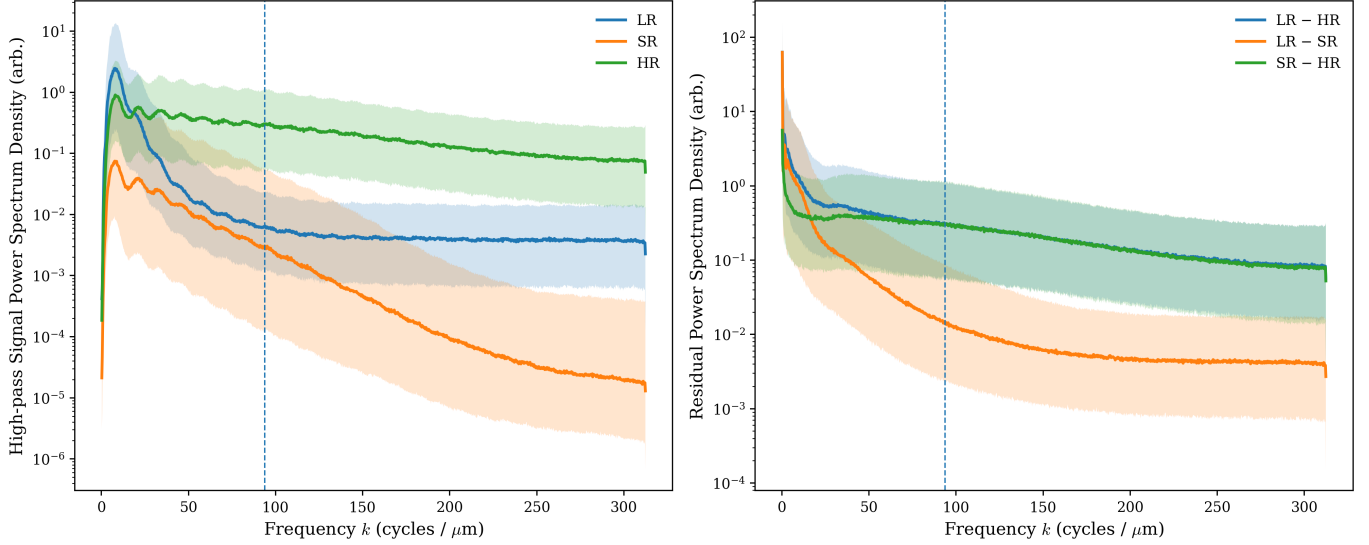


**Figure 7.** Frequency-domain diagnostics of the super-resolution performance. *Left:* Power spectral density (PSD) of the high-pass component of the spectra, computed by subtracting a smoothed continuum (window size = 101 pixels) and taking the median across objects. Solid lines show the median PSD, while shaded regions indicate the 16th–84th percentile range across the sample. The low-resolution (LR) spectra exhibit excess high-frequency power dominated by noise and undersampling effects, while the high-resolution (HR) spectra contain the richest small-scale structure. The super-resolved (SR) spectra show systematically lower high-frequency power than both LR and HR, indicating effective suppression of noise-dominated fluctuations and a conservative reconstruction that avoids injecting spurious fine-scale structure. *Right:* PSD of residuals between different spectral products, shown as median curves with 16th–84th percentile ranges. The LR–HR residuals display strong high-frequency power, whereas the LR–SR residuals are substantially reduced, demonstrating suppression of noise present in the LR data. The remaining SR–HR residual power is smooth and consistent with the noise properties of the HR spectra, suggesting that further improvement is limited by the data rather than by the model. All spectra are evaluated on a common wavelength grid for comparison; power at the highest frequencies is therefore sensitive to interpolation and should be interpreted only in a relative sense. The vertical dashed line marks  $0.3 k_{\text{Nyq}}$ , separating intermediate-scale structure from noise-dominated frequencies.

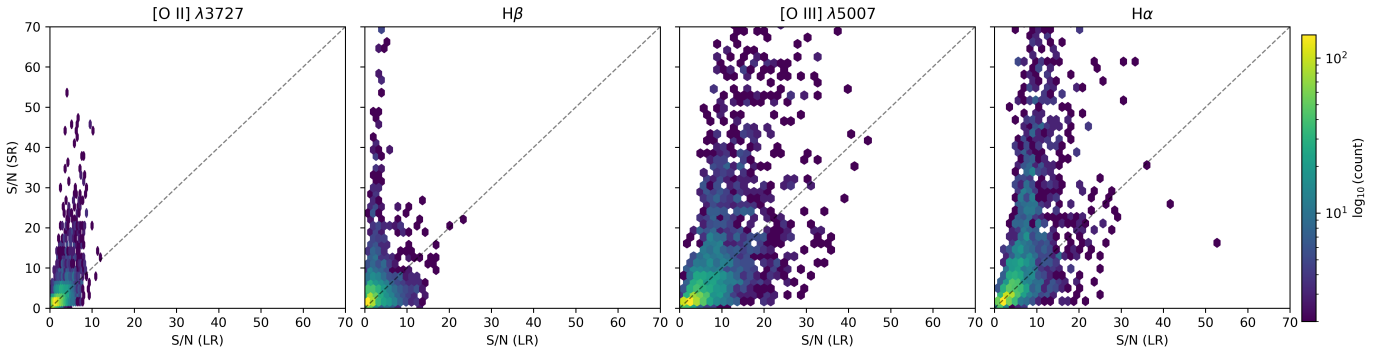


**Figure 8.** Comparison of emission-line S/N between low-resolution (LR) and super-resolved (SR) spectra for [O II]  $\lambda 3727$ ,  $H\beta$ , [O III]  $\lambda 5007$ , and  $H\alpha$ . Each point represents a single galaxy from the 20% held-out evaluation set. S/N values are obtained from Gaussian line fits (Equation 1), with the local continuum estimated from sidebands adjacent to each line. The dashed line marks the one-to-one relation. Points above this line indicate improved S/N in the super-resolved spectrum. The color scale indicates the density of points in  $\log_{10}$  counts.

#### 4.4. Redshift Consistency as a Downstream Diagnostic

Although the primary goal of this work is not redshift estimation, we use redshift consistency as an informative downstream diagnostic to assess how much physically relevant information is recovered by the SR spec-

tra. To this end, we train identical deep-learning models to predict galaxy redshifts from three different spectral inputs: the original low-resolution prism spectra (LR), the super-resolved outputs (SR), and the high-resolution reference spectra (HR). All models share the same ar-

chitecture, loss function, training procedure, and data split, such that any performance differences can be attributed solely to the information content of the input spectra.

Figure 9 compares predicted and true redshifts for the three cases. Despite the fact that the networks are not explicitly optimized for redshift accuracy, the super-resolved spectra yield a substantial improvement over the low-resolution inputs. In particular, the robust scatter  $\text{NMAD}(|\Delta z|)$  is reduced by approximately a factor of two relative to the LR case, and the fraction of catastrophic outliers decreases from  $\sim 16\%$  to  $\sim 12\%$ . Remarkably, the redshift performance obtained from the SR spectra closely approaches that achieved using the HR reference data, and in some regimes marginally surpasses it, reflecting the denoising and regularization effects of the super-resolution model.

We emphasize that these results should not be interpreted as optimized redshift measurements, nor as representative of a complete galaxy population. Rather, they provide an apples-to-apples comparison demonstrating that super-resolution recovers most of the redshift-relevant information present in the high-resolution spectra, while substantially outperforming the native prism data. This behavior is fully consistent with the improvements in emission-line recoverability presented above and highlights the potential of super-resolved spectra to enable downstream analyses that are otherwise limited by spectral resolution.

## 5. DISCUSSION

In this work, we have presented a proof of concept for deep-learning-based spectral super-resolution of galaxy spectra, demonstrating that a staged neural network trained on paired JWST/NIRSpec observations can recover emission-line features that are entirely blended at prism resolution. The model achieves noise-limited residuals over most of the spectral range, systematically improves the S/N of key diagnostic lines, and successfully deblends features such as the [O III] doublet and  $\text{H}\beta$ . While these results are encouraging, the current framework has important limitations that define the path for future development.

We adopt the NIRSpec prism ( $R \sim 100$ ) and medium-resolution grating modes ( $R \sim 1000$ ) as our low- and high-resolution pairs, rather than targeting the highest NIRSpec resolving power ( $R \sim 2700$ ). This choice is driven by data availability: truly high-resolution NIRSpec observations exist, but only over limited sky coverage, such as the NIRSpec Wide GTO Survey (Maseda et al. 2024). In contrast, JADES provides a uniquely deep and homogeneous medium-resolution dataset over

a significantly larger area, enabling statistically robust training. Our results therefore reflect the practical ceiling imposed by the available reference set. With future wide-area surveys obtained at  $R \sim 2700$ , the same framework could be retrained to deliver substantially sharper reconstructions. More broadly, the quality, size, and diversity of the training data are the primary bottleneck for this approach: improvements in the model will follow directly from improvements in the available paired spectroscopic samples.

We introduced a quality cut requiring at least one emission line detected at  $\text{S/N} > 5$  in the medium-resolution spectrum, with the understanding that this introduces a mild selection bias toward emission-line galaxies. This precaution was necessary to ensure that each training pair contains at least one real spectral feature, preventing the network from generating spurious emission features in noise-dominated spectra. As a result, our generated spectra do not exhibit false-positive emission lines in any of our tests. However, this also means the model has not been trained or evaluated on quiescent or absorption-line-dominated galaxies, and its performance on such systems remains untested. Extending the framework to absorption-line features would require a training set with sufficient numbers of high-S/N continuum-dominated spectra, which future JWST programs may provide.

Several further limitations of the current framework should be noted. The training sample of 1,187 paired spectra, while augmented to  $\sim 25,000$ , is small by machine-learning standards. The model’s ability to generalize to galaxy populations that are underrepresented in the JADES sample, such as extremely dusty systems, low-mass galaxies, or sources at the highest redshifts, has not been established. The model predicts wavelength-dependent uncertainties, but we have not yet performed a detailed calibration analysis to assess whether these uncertainties are statistically well-calibrated. Performance degrades at the bluest wavelengths ( $\lesssim 1.5 \mu\text{m}$ ), where both the prism input and the HR reference spectra have low S/N; this is a data limitation rather than a model failure, but it restricts the applicability of the current framework to rest-frame UV diagnostics at lower redshifts. Finally, we note that this approach should be understood as applying a learned prior from the training data rather than recovering information that is truly present in the low-resolution input. The model cannot reconstruct features that have no statistical relationship with the prism data; its power lies in exploiting correlations learned from the paired sample.

Despite these limitations, the framework has significant potential for both galaxy evolution and cos-

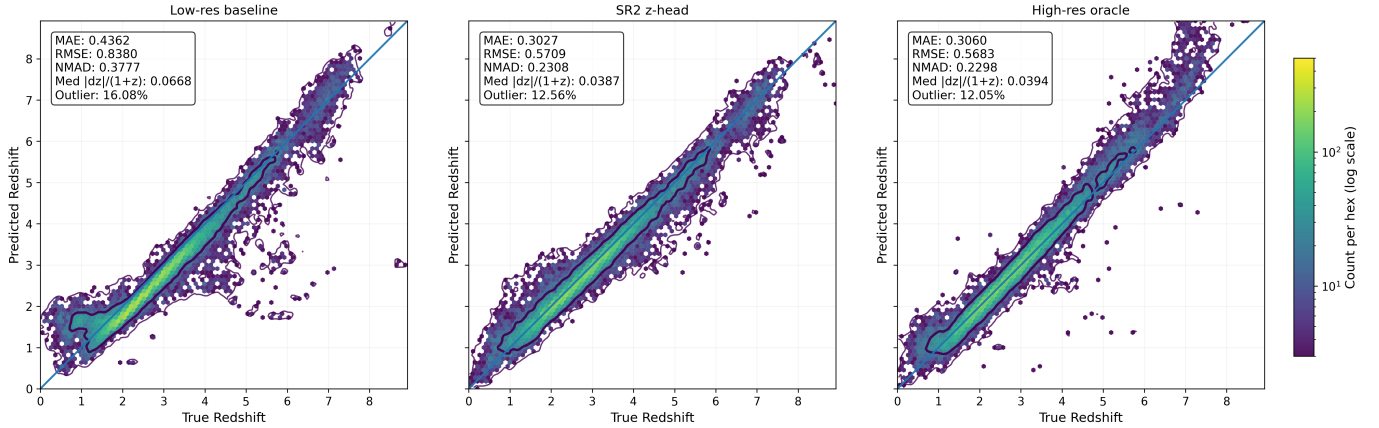


**Figure 9.** Comparison of predicted and true redshifts obtained from identical deep-learning models trained on three different spectral inputs: low-resolution prism spectra (left), super-resolved spectra produced by our model (middle), and high-resolution reference spectra (right). All panels use the same axis limits and color normalization, and show the one-to-one relation (solid line). The shaded hexagonal density indicates the distribution of galaxies in the held-out evaluation set, while the contours enclose the 68% (thick) and 95% (thin) highest-density regions. Although the networks are not explicitly optimized for redshift estimation, the super-resolved spectra yield a substantial reduction in scatter and outlier fraction relative to the low-resolution input, approaching the performance achieved using the high-resolution reference data. This comparison provides an apples-to-apples diagnostic of the information content recovered by the super-resolution model, rather than a measurement of optimal redshift performance.

mological studies. High-resolution spectra are essential for refining fundamental scaling relations such as the star-formation rate–stellar mass relation, the mass–metallicity relation, and the BPT diagnostic diagram. Current JWST studies demonstrate that limited sample sizes and resolution effects bias these relations toward bright, spectrally resolved galaxies (e.g., Clarke et al. 2024; Laseter et al. 2024; Nakajima et al. 2023; Scholte et al. 2025). By enabling high-resolution diagnostics for statistically larger samples, our approach has the potential to reduce these biases. For example, blended line measurements can blur the separation between star-forming and AGN populations on the BPT plane (Agostino et al. 2023), and empirical corrections for the  $[\text{N II}]/\text{H}\alpha$  ratio introduce substantial scatter and systematic uncertainty (Faisst et al. 2018). A model that directly recovers these blended features from prism data could eliminate the need for such approximations, enabling cleaner classification and more accurate physical parameter estimates across large samples.

Improved emission-line S/N from super-resolved spectra also has direct consequences for cosmological analyses. More precise and unbiased redshift measurements strengthen galaxy clustering studies, while an expanded sample of galaxies with well-measured  $\text{H}\alpha$  increases the statistical power of large-scale structure analyses, tightening constraints on cosmological parameters and the growth of structure (e.g., Laureijs et al. 2011). By learning physically consistent line profiles from paired JWST data, the model could in principle be applied to large-

area grism surveys without requiring additional follow-up spectroscopy, effectively producing high-resolution spectral information at a fraction of the observational cost.

As discussed in §1 and §2, the broad wavelength coverage of the JADES training data makes this framework readily extensible to low-resolution grism spectroscopy from *Euclid* and the *Roman Space Telescope*. However, applying the model to these datasets will require careful attention to domain shift: differences in instrumental noise properties, spectral resolution profiles, and wavelength coverage between NIRSpec and grism spectrometers may degrade out-of-the-box performance. Addressing this will likely require some combination of fine-tuning on instrument-specific simulations or small calibration samples, and potentially domain adaptation techniques.

Looking further ahead, several avenues could substantially improve the framework. Incorporating broadband photometry as an additional input channel would provide complementary constraints on continuum shape, stellar mass, and redshift that are not available from the low-resolution spectrum alone. The recent development of foundation models for astronomical data offers a promising direction here, as pretrained representations of galaxy spectral energy distributions could serve as powerful priors for the super-resolution task (Parker et al. 2025). Expanding the training set through future JWST programs, particularly those targeting higher spectral resolution ( $R \sim 2700$ ) over wider areas, would

directly improve reconstruction fidelity. Finally, extending the model to handle absorption-line features and continuum diagnostics would broaden its applicability to the full diversity of galaxy populations observed in current and upcoming surveys.

## 6. ACKNOWLEDGMENTS

We thank *Jeffrey W. Kruk*, *Motahareh Pourrahimi*, and *Vladimir Vuskovic* for their valuable comments during the preparation of this manuscript. This work does not relate to the positions of Hooshang Nayyeri at Amazon.

## REFERENCES

- Adame, A. G., Aguilar, J., Ahlen, S., et al. 2025, JCAP, 2025, 021, doi: [10.1088/1475-7516/2025/02/021](https://doi.org/10.1088/1475-7516/2025/02/021)
- Agostino, C. J., Salim, S., Boquien, M., et al. 2023, Monthly Notices of the Royal Astronomical Society, 526, 4455
- Alavi, A., Siana, B., Teplitz, H. I., et al. 2026, ApJ, 997, 290, doi: [10.3847/1538-4357/ae2473](https://doi.org/10.3847/1538-4357/ae2473)
- Baldwin, A., Phillips, M., & Terlevich, R. 1981, Publications of the Astronomical Society of the Pacific, 93, 817
- Biewald, L. 2020, Experiment Tracking with Weights and Biases, <https://www.wandb.com/>
- Bunker, A. J., Cameron, A. J., Curtis-Lake, E., et al. 2024, Astronomy & Astrophysics, 690, A288
- Clarke, L., Shapley, A. E., Sanders, R. L., et al. 2024, The Astrophysical Journal, 977, 133
- Curtis-Lake, E., Cameron, A. J., Bunker, A. J., et al. 2025, arXiv e-prints, arXiv:2510.01033, doi: [10.48550/arXiv.2510.01033](https://doi.org/10.48550/arXiv.2510.01033)
- Darvish, B., Mobasher, B., Sobral, D., et al. 2015, ApJ, 814, 84, doi: [10.1088/0004-637X/814/2/84](https://doi.org/10.1088/0004-637X/814/2/84)
- Djorgovski, S. G., Mahabal, A., Graham, M. J., Polsterer, K., & Krone-Martins, A. 2022, arXiv preprint arXiv:2212.01493
- Donald, E., & Osterbrock, F. 2005, Astrophysics of Gaseous Nebulae and Active Galactic Nuclei (University Science Books)
- Doorenbos, L., Sextl, E., Heng, K., et al. 2024, The Astrophysical Journal, 977, 131
- D'Eugenio, F., Cameron, A. J., Scholtz, J., et al. 2025, The Astrophysical Journal Supplement Series, 277, 4
- Eisenstein, D. J., Willott, C., Alberts, S., et al. 2023, arXiv preprint arXiv:2306.02465
- Eisenstein, D. J., Johnson, B. D., Robertson, B., et al. 2025, The Astrophysical Journal Supplement Series, 281, 50
- Faisst, A. L., Masters, D., Wang, Y., et al. 2018, The Astrophysical Journal, 855, 132
- Gardner, J. P., Mather, J. C., Clampin, M., et al. 2006, Space Science Reviews, 123, 485
- Giavalisco, M., Ferguson, H., Koekemoer, A., et al. 2004, The Astrophysical Journal, 600, L93
- Haghjoo, A. 2023, Parameter Estimation of the Global 21cm Signal (McGill University (Canada))
- Hartigan, P., Raymond, J., & Pierson, R. 2004, The Astrophysical Journal, 614, L69
- Hemmati, S., Capak, P., Masters, D., et al. 2019, ApJ, 877, 117, doi: [10.3847/1538-4357/ab1be5](https://doi.org/10.3847/1538-4357/ab1be5)
- Hemmati, S., Huff, E., Nayyeri, H., et al. 2022, The Astrophysical Journal, 941, 141
- Hemmati, S., Krick, J., Stern, D., et al. 2026, The Astrophysical Journal, 998, 130
- Howard, A. G., Zhu, M., Chen, B., et al. 2017, MobileNets: Efficient Convolutional Neural Networks for Mobile Vision Applications. <https://arxiv.org/abs/1704.04861>
- Ji, X., Yan, R., Riffel, R., Drory, N., & Zhang, K. 2020, Monthly Notices of the Royal Astronomical Society, 496, 1262
- Kewley, L. J., Groves, B., Kauffmann, G., & Heckman, T. 2006, Monthly Notices of the Royal Astronomical Society, 372, 961
- Khostovan, A. A., Malhotra, S., Rhoads, J. E., et al. 2024, MNRAS, 535, 2903, doi: [10.1093/mnras/stae2395](https://doi.org/10.1093/mnras/stae2395)
- Kollmeier, J. A., Rix, H.-W., Aerts, C., et al. 2026, The Astronomical Journal, 171, 52
- Lallo, M., & Hartig, G. 2022, Technical Report JWST-STScI-008271, 8271
- Laseter, I. H., Maseda, M. V., Curti, M., et al. 2024, Astronomy & Astrophysics, 681, A70
- Laureijs, R., Amiaux, J., Arduini, S., et al. 2011, arXiv preprint arXiv:1110.3193
- Laureijs, R. J., Duvet, L., Sanz, I. E., et al. 2010, in Space Telescopes and Instrumentation 2010: Optical, Infrared, and Millimeter Wave, Vol. 7731, SPIE, 453–458
- Martens, D., Fang, X., Troxel, M., et al. 2019, Monthly Notices of the Royal Astronomical Society, 485, 211
- Martini, P., Bailey, S., Besuner, R. W., et al. 2018, in Ground-based and Airborne Instrumentation for Astronomy VII, Vol. 10702, SPIE, 410–420
- Maseda, M. V., de Graaff, A., Franx, M., et al. 2024, Astronomy & Astrophysics, 689, A73
- Nakajima, K., Ouchi, M., Isole, Y., et al. 2023, The Astrophysical Journal Supplement Series, 269, 33

- Parker, L., Lanusse, F., Golkar, S., et al. 2024, *Monthly Notices of the Royal Astronomical Society*, 531, 4990
- Parker, L., Lanusse, F., Shen, J., et al. 2025, arXiv preprint arXiv:2510.17960
- Price, S. H., Kriek, M., Barro, G., et al. 2020, *The Astrophysical Journal*, 894, 91
- Rieke, M. J., Robertson, B., Tacchella, S., et al. 2023, *The Astrophysical Journal Supplement Series*, 269, 16
- Sanjaripour, S., Hemmati, S., Mobasher, B., et al. 2024, *The Astrophysical Journal*, 977, 202
- Schlieder, J. E., Barclay, T., Barnes, A., et al. 2024, in *Space Telescopes and Instrumentation 2024: Optical, Infrared, and Millimeter Wave*, Vol. 13092, SPIE, 196–221
- Scholte, D., Cullen, F., Carnall, A., et al. 2025, *Monthly Notices of the Royal Astronomical Society*, 540, 1800
- Schreiber, N. F., Genzel, R., Bouché, N., et al. 2009, *The Astrophysical Journal*, 706, 1364
- Shen, L., Papovich, C., Matharu, J., et al. 2025, *ApJL*, 980, L45, doi: [10.3847/2041-8213/adb28d](https://doi.org/10.3847/2041-8213/adb28d)
- Shivaei, I., Kriek, M., Reddy, N. A., et al. 2016, *ApJL*, 820, L23, doi: [10.3847/2041-8205/820/2/L23](https://doi.org/10.3847/2041-8205/820/2/L23)
- Shivaei, I., Reddy, N., Rieke, G., et al. 2020, *ApJ*, 899, 117, doi: [10.3847/1538-4357/aba35e](https://doi.org/10.3847/1538-4357/aba35e)
- Sobral, D., Best, P. N., Geach, J. E., et al. 2009, *MNRAS*, 398, 75, doi: [10.1111/j.1365-2966.2009.15129.x](https://doi.org/10.1111/j.1365-2966.2009.15129.x)
- Spergel, D., Gehrels, N., Breckinridge, J., et al. 2013, arXiv preprint arXiv:1305.5425
- Wang, Y., Dickinson, M., Hillenbrand, L., et al. 2019, arXiv e-prints, arXiv:1909.00070, doi: [10.48550/arXiv.1909.00070](https://doi.org/10.48550/arXiv.1909.00070)
- Woodrum, C., Shivaei, I., Witstok, J., et al. 2025, arXiv e-prints, arXiv:2510.00235, doi: [10.48550/arXiv.2510.00235](https://doi.org/10.48550/arXiv.2510.00235)